Wear 530-531 (2023) 205020

Contents lists available at ScienceDirect

Wear

journal homepage: www.elsevier.com/locate/wear

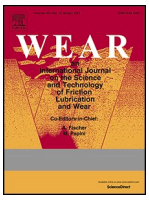

Multiscale simulation of volumetric wear of vitrified alumina grinding wheels

T. Pazmiño [a,c,*], I. Pombo [a], J. Girardot [b], L. Godino [a], J.A. Sánchez [a]

[a] Faculty of Engineering Bilbao, University of the Basque Country (UPV/EHU), Plaza Torres Quevedo, 1, Bilbao, 48013, Spain
[b] Arts et Metiers Institute of Technology, CNRS, Bordeaux INP, Hesam Universite, I2M, UMR 5295, Talance, F-33400, France
[c] University of Bordeaux, CNRS, Bordeaux INP, I2M, UMR 5295, Talance, F-33400, France

A B S T R A C T

Wear of vitrified alumina wheels is a major research issue. Although extensive experimental work has been presented in the scientific literature, wheel manufacturers and grinding users are still unable to predict the expected grinding ratio of their operations. This work presents a novel multiscale approach that integrates the mechanical behavior of vitrified bonds with the stochastic nature of grain location. The new multiscale model integrates a DEM microscale model (μSM) and a randomization of the μSM ($R\mu SM$) of the wheel. The μSM simulates the stress field in the region of the wheel in contact with the workpiece, while $R\mu SM$ accounts for the actual and random location of the alumina grits. This approach drastically reduces computational time and effectively determines the actual number of grains lost under a set of given grinding conditions. The model successfully predicts the detachment of complete clusters of abrasive grains from the bonds, with a large degree of agreement with experiments considering the deviation introduced by the micro-cutting edges that modify the hypothetical spherical geometry of the Discrete Elements (DEs). This is the first model to predict the volumetric wear of grinding wheels. The results will be useful for informing the future analysis of grinding operations affected by volumetric wear.

1. Introduction

High-technology manufacturing sectors recognize that the grinding process is a key technology for the production of high added-value parts [1]. Cutting-edge industrial applications include the finishing of turbine blade roots or landing gears in aeronautic industry [2], transmission gears for the automotive industry [3] or critical parts in the machine-tool or marine industry [4]. In some cases, there is a need for high material removal rates (comparable to those of milling), together with high geometrical and dimensional precision, and extreme surface quality [5]. The growing need for tight tolerances and excellent surface finish in difficult-to-machine materials such as nickel-based super alloys [6], titanium alloys [7] or hardened steels [8] has also encouraged the development of advanced grinding applications. Although many of those applications are well suited to super abrasive grinding, the recent advances in vitrified alumina grinding wheels allow for considering this option as an optimum solution. The advantages of vitrified alumina technology include a lower cost when compared to super abrasive wheels; the improved performance of the latest developments of alumina grains [9]; a much more efficient dressing/trueing process of vitrified alumina [10]; and excellent performance in creep-feed grinding applications [2] since their controlled porosity can effectively support chip removal. Conversely, brittleness and increased risk of bond breakage are the main disadvantages.

The wear of vitrified alumina wheels is an issue of central concern for researchers. Classic grinding references [11] have identified three main wear mechanisms: attritious wear, grain fracture, and bond fracture. These phenomena are explained in terms of high local pressures (1–2 GPa), temperatures, and the chemical reactions between wheel and workpiece. The performance of a vitrified alumina wheel would thus depend on grit type and size, and the quantity, type, and porosity of the bond. Bond fracture is related to volumetric wear, which is classically quantified using the grinding ratio G. The scientific literature has gathered evidence to show that bond fracture, and therefore, volumetric wear, are related to the breakage of vitreous bond bridges. In the 70's, Malkin and Cook [11] had already proposed using a bond-stress factor to account for the probability of fracture of the vitreous bridges. One of the most significant contributions toward fully understanding vitreous bonds was published by Jackson [12]. This study was conducted to determine the effect of the sintering treatment on the mechanical behavior of vitreous bonding. In the case of vitrified alumina, the author observed fractures at the bridges and on the interface between the abrasive grit and the vitreous material. The author confirmed that the theory of brittle fracture is valid for vitreous bonding. Further, evidence was found for an association between the dressing operation and the

* Corresponding author. Faculty of Engineering Bilbao, University of the Basque Country (UPV/EHU), Plaza Torres Quevedo, 1, Bilbao, 48013, Spain.
E-mail addresses: tyrone.pazmino@ehu.eus, tyrone_pazmino_86@hotmail.com (T. Pazmiño).

https://doi.org/10.1016/j.wear.2023.205020
Received 17 April 2023; Received in revised form 1 June 2023; Accepted 9 June 2023
Available online 26 June 2023

Nomenclature

a_e	real depth of cut (mm)
a_{ed}	dressing depth of cut (mm)
d_e	grinding wheel diameter (mm)
d_g	average grain diameter (mm)
d_{gmax}	maximum grain diameter (mm)
d_{gmin}	minimum grain diameter (mm)
DEs	spherical discrete elements
DEM	discrete element method
e_c	specific grinding energy (J/mm^3)
E^*	combined elastic properties of the grinding wheel and workpiece (GPa)
E_s, E_μ	grinding wheel and beam Young modulus (GPa)
f_{cj}	centrifugal force in each DE (N)
F_n, F_t	normal and tangential grinding force (N), tangential grinding force (N)
F_n', F_t'	normal and tangential grinding force per unit width (N/mm)
$F_{n\ new}'$	new normal grinding force per unit width (N/mm)
$F_{t\ new}'$	new tangential grinding force per unit width (N/mm)
G	grinding ratio
h_s	height of microscale model (mm)
K	contact stiffness (N/m)
l_c	contact length (mm)
l_f	dynamic contact length (mm)
l_g	geometrical contact length (mm)
L_μ	beam length in DEM (mm)
m	grinding wheel mass (Kg)
m_j	mass of each DE (Kg)
M	sieve number
$N_{r\ new}$, N_r	new number and number of discrete elements removed
P'	specific power (KW/mm)
Q_w'	specific metal removal rate (mm^3/mm·s)
q_s	velocity ratio
r_j	distance from the center of each DE to the center of the wheel (mm)
r_μ	ratio between cohesive beam radius and average DE radius
R_j	distance from the outermost grain to the center of the *RμSM* (mm)
R_r	roughness factor
RμSM	randomization of the *μSM*
U_d	dressing overlap
v_d	dressing axial feed (mm/min)
V_g	abrasive volume fraction (%)
V_p	porosity volume (%)
v_s	cutting speed (m/s)
V'_s	specific volumetric wear (mm^3/mm)
v_w	work speed (m/s)
V'_w	specific volume of metal removed (mm^3/mm)
S_f	grain shape factor
w	grinding width (mm)
δ_{av}	average grit penetration (mm)
δ_{cnew}, δ_C	new and critical grit penetration (mm)
δ_{max}	maximum grit penetration (mm)
υ_s, υ_μ	grinding wheel and beam poisson ratio
Δ	radial wear (mm)
σ	normal tension of beams in DEM (MPa)
τ	tangential tension of beams in DEM (MPa)
ρ	grinding wheel density (Kg/m^3)
σ_f, $\sigma_{f\mu}$	grinding wheel and DEM beam failure stress (MPa)
μ	friction coefficient
μSM	microscale modelω rotational speed of the grinding wheel (rad/s)

initial presence of microcracks. The generation of cyclic thermo-mechanical loads during grinding would thus lead to crack propagation, and eventually, bond fracture.

In a later study, Herman and Markul [13] examined the influence of vitrified bond composition on the minimization of volumetric wear. Their experimental findings revealed that a glass-crystalline bond could increase the *G* ratio 10 times when compared with that of a common glass bond. Glass-crystalline bonds promote microchipping as the main wear mechanism in the bond. In contrast, the amorphous structure of conventional vitreous bond characterized by the absence of intergranular boundaries is responsible for much lower values of fracture toughness (as much as 3 times lower than those of a glass-crystalline bond structure). The authors modelled this result by modifying Griffith's equation, results that were later confirmed for CBN wheels [14]. In this work, the radial wear using a glass-crystalline bond was around 28% lower than that using conventional glass bond. The experimental nature of the research provides a better understating of the mechanical properties of the bonds.

More recently, experimental works have confirmed previous findings on the nature of volumetric wear. In Ref. [15], the accuracy of characterizing the grinding profile of the inner ring groove of 6208 ball bearings was studied. The authors developed a new pneumatic probe for on-line measurement of wheel wear, in which the sensor is validated using a vitrified white fused alumina (A100L5V) profiled wheel. The results revealed an uneven distribution of wear that affects part accuracy. While the various wear mechanisms were present, a high wear rate was observed during the initial stage of grinding, since entire abrasive grains are readily emitted from the bond. A complete analysis of wear patterns for different types of vitrified alumina wheels during creep-feed grinding of Ni-based superalloys can be found in Ref. [16]. Again, the authors acknowledged the role of the different types of wear and found that for low removal rates, wear is largely governed by the occurrence of attritious wear, workpiece adhesion and wheel loading. However, when increasing *Q'*, the mechanism changed, and clear evidence of grain fracture and bond bridge fracture appeared. The dominant wear mechanism depends on the aggressiveness of the grinding process. Thus, fracture wear is not dominant when the grinding conditions are not aggressive (e.g., in finishing) where the wear is primarily attritious. In Ref. [2], the research focused on the effect of wheel wear in the grinding of fir-tree geometries for turbine blade roots. Profiled vitrified microcrystalline alumina wheels were used for the creep-feed grinding of Ni alloy. The authors demonstrated that wear is more concentrated around wheel peak regions than valley regions. As expected, different wear mechanisms overlap, but fracture of bond bridges is recognized as a critical phenomenon in the wheel peak regions. The authors developed an experimental model for wheel wear prediction for this application, but without considering the mechanical properties of grains and vitrified bond.

The development and application of theoretical models for the behavior of the bond bridges during grinding requires sound experimental characterization of the mechanical properties of the wheel material. These properties, such as elastic modulus and ultimate strength, can be measured through three and four-point bending tests. The Brazilian test is a widely employed indirect method used for determining the tensile strength of brittle materials, including ceramics, concrete, rocks, and composites. During the Brazilian test, a cylindrical specimen is positioned between two compressive loading platens. By applying a diametrical compressive force to the specimen, it is subjected to conditions that induce tensile stresses perpendicular to its vertical diameter. This setup allows for the evaluation of the specimen's tensile strength

through its failure. Brazilian and compression tests have been proposed to measure the ultimate strength of the composite body of the grinding wheel [17]. This information was then used by the authors as input for stress analysis of the vitrified binder during grinding. They propose a discontinuous body hypothesis which formed the basis of a Discrete Element Model of the grinding wheel that will be discussed later in this section.

A very complete review of experimental test to characterize wheel wear behavior can be found in Ref. [18]. The fracture strength and the Weibull modulus are also common parameters used to study porous brittle materials [19] because the latter describes the variability observed in the experiments. The nature and structure of vitrified alumina grinding wheels resembles, to a certain extent, those of brittle porous materials. Therefore, interesting analogies can be found. In the same study [19], the authors used the Brazilian tests and a Lattice Spring Model (LSM) to examine the influence of pore size and distribution on the fracture strength of the material. They concluded that the Weibull modulus shows significant variations for porosities around 10%, while a constant value was found for porosities higher than 20%. Moreover, for a porosity lower than 10%, the Weibull modulus is more sensitive to the increments in pore size. This study also shows that porosity has a greater influence on fracture strength than pore size. The scientific literature and industrial practice also show that the porosity of vitrified alumina grinding wheels can vary from 1% up to 50% [20,21] depending on the application and grain shape. These findings must therefore be considered when carrying out experiments to characterize the mechanical behavior of grinding wheels.

The Brazilian test also deserves special attention. This test is a commonly-accepted experimental technique for determining the maximum strength of brittle materials. The most common shape of a Brazilian test specimen is a disk using a curve-bearing block to apply the compression force. For brittle materials, Bahaaddini et al. [22] demonstrated the influence of specimen geometry and contact area on the stress value and its distribution in the disk on Brazilian tests. Likewise, they highlighted that the failure mechanisms could vary depending on those factors. In their work, the contact loading angle varied from 1° to 30°, leading the authors to conclude that the most robust set-up is obtained with angles higher than 30°. Zhang et al. [23] conducted an experimental analysis of tensile stress using a modified Brazilian test for nuclear graphite, also varying the contact angle by up to 30°, showing that the crack initiates in the contact area. Thus, for a better understanding of fracture behavior, it is necessary to avoid the crack initiation in the contact area and to promote crack initiation in a predetermined zone. To tackle this issue, Ayallatolaghi et al. [24] analyzed the influence of V-notched polycrystalline graphite specimens on crack initiation, varying the size and the angle of the notch. They obtained the mixed fracture Mode I and II both theoretically and experimentally. Likewise, they demonstrated the influence of the notched angle on crack initiation. Therefore, test set-up and sample geometry must be considered critical for obtaining accurate values.

In addition to the maximum strength value, the location of crack initiation and its evolution under the applied force is also of interest for characterizing mechanical behavior. To evaluate crack propagation in the fracture zone, the Digital Image Correlation (DIC) technique has been proposed [25,26]. DIC analysis provides quality information on crack behavior just at the crack tip and also measures the correlation between applied load, crack length, and propagation speed.

Together with material properties, it is important to consider the forces exerted on the wheel and the loads transmitted to the binder during the grinding process. Classical research works [27,28] have acknowledged the role of stress distribution in the binder and its effect on the elasticity and deformations of the grinding wheel. Later, a probabilistic model based on the concept of the undeformed chip thickness was proposed by Hecker in Ref. [29]. Other investigations have shown that the nature of the contact between the abrasive grains and the workpiece is very complex [30] and includes continuous variation of the friction coefficient and local contact stiffness. In Ref. [31] the authors proposed a model for forces and energy partition based on the nature of the different types of contact between grit and workpiece, which allowed for gaining a qualitative insight into the loads imposed on the binder. However, little or no information can be found in the above works regarding the relationship between the binder's mechanical properties and volumetric wear of the wheel.

Numerical methods provide a powerful tool for studying the mechanical behavior of porous brittle materials. These include the Discrete Element Method (DEM), which has been successfully used to simulate both Brazilian and triaxial tests on geomaterials and concrete [32]. Concerning vitrified grinding wheels, an interesting analysis of the loads on the binder was presented in the already mentioned work by Li et al. [17]. The original contribution of this work is the use of the discontinuum-hypothesis-based grinding simulation using DEM. In this work, the authors describe the basis for calculating the stresses on the binder of the grinding wheel. The model considers various grit geometries and discretization of both abrasive and vitreous bond. Because of the high computational cost, the model is limited to the contact region between wheel and workpiece, and the wheel material is characterized using Brazilian tests. Finally, grinding tests were conducted to validate the model, measuring grinding forces and final part topography. The authors completed their research in a subsequent article [33]. Although their work did not consider volumetric wear and G ratio, their proposals have paved the way for efficient characterization and simulation of the behavior of vitreous bonds.

In this context, the work by Osa et al. [34] must also be mentioned. In their research, the authors modelled the wheel using the discontinuous body hypothesis in which the abrasive grains are the discrete elements, and the binder is represented by elastic beams. The actual complex geometry of the grains can be successfully simplified using spheres with little error, which considerably reduces computational cost. Moreover, the use of beams for the binder represents a significant advance in this direction. The authors calculated the stress distribution on the binder, which in turn allowed for quantifying the elastic deformations on the wheel that are caused by the grinding forces. The model was validated through calculation of the contact length and comparison of this value with existing references. One of the most relevant findings of this work is the significant impact of the active number of grains on the contact stiffness and, therefore, on the stresses on the binder. The use of different dressing strategies reveals and highlights this critical point. Again, the model does not consider fracture of bond bridges, since volumetric wear and prediction of G ratio lie outside the scope of that research. However, tribological studies in the scientific literature have revealed the efficiency of DEM for describing fracture mechanics [35].

Another notable contribution is the work by Spampinato and Axinte [36]. These authors presented a method for predicting the output forces and topography (grit size and protrusion) of a simulated grinding wheel during dressing operations. The method involves the contact between two rotating bodies with statistically distributed abrasive grains, taking into account the abrasive characteristics of both bodies. The model simulates the collisional effects of the dresser abrasives on the grinding wheel's topography. Experimental calibration was conducted to account for the deflection in the abrasive contact, assuming a kinematic contact length. The model uses the DEM to simulate the abrasive structures and interactions. The underlying derivations are related to actual and critical stress of an individual grit in the contact. The model's results were validated against experimental data obtained from dressing operations under various operational parameters. The study focused on investigating the dominant mechanisms governing the dressing operation, with grain fracture being identified as the predominant mechanism. Additionally, the kinematic contact length was found to increase with the equivalent diameter and feed-rate, resulting in a greater number of particles involved in the collisional process. Moreover, it was clarified that the forces were directly related to the contact area, considering the effects of deflection.

This review of the scientific literature suggests that there are still important aspects to be addressed to gain a better understanding of the nature of volumetric wear of vitrified grinding wheels. This study presents, for the first time, an original multiscale approach that integrates the mechanical behavior of vitrified bonds together with the stochastic nature intrinsic to grain location. The objective of the multiscale numerical model is to explain the underlying causes of volumetric wear and to predict the value of the grinding ratio *G*. To this end, the new multiscale model integrates a DEM microscale model (*μSM*) and a *RμSM* (randomization of the *μSM*). The DEM *μSM* simulates the stress field in the region of the wheel in contact with the workpiece. The inputs to the *μSM* are the grinding forces measured in experiments and the mechanical properties of the wheel material. The geometrical randomization of the *μSM* accounts for the actual (and to a certain extent) random location of the alumina grits. Following this approach, it is possible to drastically reduce computational time and effectively determine the actual number of grains lost while also examining the role played by the apparent hardness of the grinding wheel. To the best of our knowledge, this is the first model to quantify the effect of grinding parameters on the hardness of the wheel. The layout of this paper is as follows: Section 2 presents the theoretical foundations of the original multiscale simulation model. Section 3 introduces the experimental methodology and the results of the grinding tests employed to determine the grinding forces, the absolute values of volumetric wear, and the *G* ratio of the vitrified bonded alumina wheel. In Section 4, the calibration of the model and the results of different virtual experiments (numerical simulations) are discussed, and then validated in light of the experiments presented in Section 3. The model successfully predicts the detachment of complete clusters of abrasive grains from the vitrified bond with a large degree of agreement with experiments, considering the deviation introduced by the micro-cutting edges that modify the hypothetical spherical geometry of the Discrete Elements (DEs). This is the first model to predict volumetric wear of grinding wheels, and the results reported here will be useful for the future analysis of grinding operations affected by volumetric wear.

2. Description of the multiscale simulation model

2.1. Overall description of the model

Volumetric wear is governed by the mechanical properties of the vitrified bond and the stochastic nature of the location of the abrasive grains. Whichever model is proposed, it must account for both fundamental factors. Due to the high computational costs involved, it would be unfeasible to develop a complete DEM model of the grinding wheel that could simulate all the grains on the wheel surface, together with all the bonding bridges between abrasive grains. Therefore, it has been decided to produce a multiscale model composed of two parts. First, a microscale model is used (*μSM*) to represent the mechanical behavior of any region of the grinding wheel. Following research by Osa et al. [34], the discontinuous body hypothesis was adopted, in which the abrasive grains are modelled as spherical discrete elements (DEs), and the binder is represented by elastic beams. However, the *μSM* alone cannot describe the wear behavior of the wheel, because of the stochastic nature of the location of grains and bond bridges. Therefore, the second part of the model consists of a *RμSM* (randomization of the *μSM*) that contains the complete geometrical information about the location of all the abrasive grains of the grinding wheel. In the following sections, both the *μSM* and the *RμSM* are described in further detail.

2.2. DEM microscale simulation model (μSM)

As stated previously, the microscale model (*μSM*) represents the mechanical behavior of any region of the grinding wheel. The model is based on the discontinuous body hypothesis in which the abrasive grains are modelled as spherical discrete elements (DEs), and the binder is represented by elastic beams.

2.2.1. Fundamentals of the DEM microscale model (μSM)

A GranOO workbench was used to develop the *μSM*. GranOO is a collection of C++/Phyton libraries and tools based on the description of the physical states of every discrete element [37]. The fact that the phenomenon of bond fracture can be efficiently described from a numerical point of view using DEM was critical when selecting the numerical method.

The physical phenomenon of wear due to bond fracture is numerically simulated by separation of discrete elements (DEs) from the *μSM*. For this, the numerical model must adequately represent the mechanical properties of the grinding wheel as well as the randomness in grain size and distribution. The hypothesis set out in this work is that bond fracture is related to the fracture of the vitrified bond, which is considered a continuous material (3D cohesive beam model). One of the advantages of the beam cohesive bond is to produce a more realistic fracture pattern [38]. As explained above, the DEs represent the abrasive grains, and the beams represent the vitrified bond bridges (see Fig. 1a). In order to describe the mechanical behavior of the cohesive beam, the Euler-Bernoulli beam theory was used. The cohesive beam model has beams that provide stiffness to the model, thus forming bridges between DEs. The beams have no mass; instead, the total mass of the wheel body is attributed to DEs. The behavior of a beam is defined by four parameters: two mechanical properties (Young's modulus E_μ and Poisson's ratio ν_μ) and two geometrical parameters (radius r_μ and length L_μ). The diameter of the beam is represented by r_μ. L_μ is defined by the distance between the centers of the DEs. These parameters are considered microscopic parameters, because of the scale of DEs and their interaction with their neighbors. Further, the position of each DE varies in each iteration, depending on the interaction of forces and torque reactions acting between them, as shown in Fig. 1b. The forces and moments of contact generate tensile bending and torsion loading on the beams causing normal stress (tensile and bending loading) and shear stress (torsion loading). The complete DEM model is provided with elasticity following the flow-chart applied by Osa [34] for calibrating the micro-scale properties of the beams, which is based on the method established by André et al. [38]. The procedure involves an iterative process based on virtual tensile testing of specimens until achieving convergence between micro and macro properties of the sample.

2.2.2. Modelling wheel structure

2.2.2.1. Radius and mass distribution of DEs. Grain diameter is measured from images captured with the optical microscope Dino-Lite Digital ProX (AM4013) at 30x, as shown in Fig. 2a. In the case of the wheel used in the experiments described in Section 3 (MA46EF12V), the result is a normal distribution with average grain diameter d_g 0.360 mm (see Fig. 2b). This distribution allows for determining maximum and minimum values of grain diameter (d_{gmax}, d_{gmin}) [39]. The results differ slightly from the value obtained using Eq. (1)), which, for the same wheel, yields a value of 0.330 mm as average grain diameter. Eq. (1)) was first proposed by Malkin [40]. In this expression, *M* is the sieve number. Fig. 2b shows that 29% of the samples exhibit grain diameters ranging from 0.33 to 0.38 mm. The lower limit (0.33 mm) corresponds to the value obtained from Eq. (1) (Malkin). It must be considered that for the measurement, the circumscribed diameter has been used. Considering the actual shape of the grains, this causes an increase in the measured diameter with respect to the value provided by the sieve number (*M*). Of course, this introduces a simplification related to the shape of the grains, which will be commented on later in Section 4.4.

$$d_g = \frac{15.2}{M} \tag{1}$$

Using the above data, the numerical sintering method [38] was used to build the *μSM*, which adequately represents the properties of

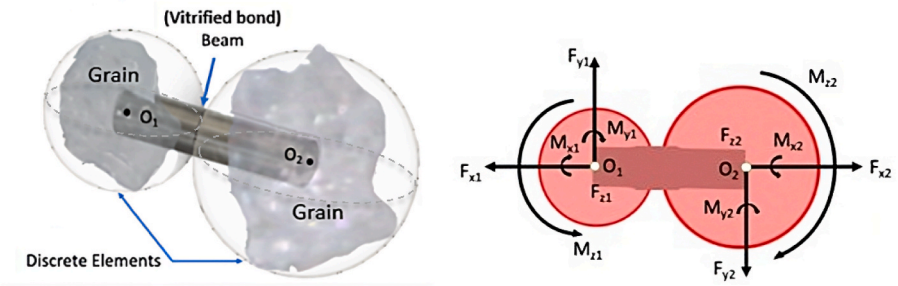

Fig. 1. Concept of cohesive beams: (a) DEs and beam representing abrasive grains and vitreous bonds respectively; (b) System of forces and torques acting between two DEs.

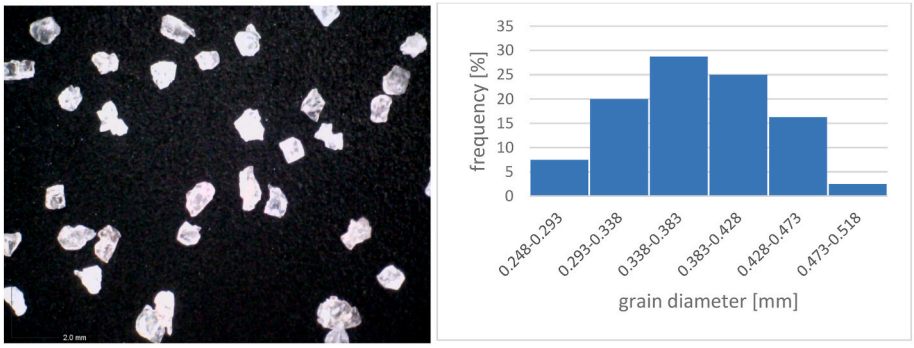

Fig. 2. Results for the wheel (MA46EF12V) used in the experiments described in Section 3. a) Alumina grains observed under a microscope (30x); b) Experimentally obtained normal distribution of grain diameter.

randomness, homogeneity, and isotropy of the actual grinding wheel. The conditions used for building the model were:

- The volumetric density of grains in the numerical domain and in the grinding wheel must be the same.
- The mass density of the numerical body and that of the grinding wheel must be the same.
- The size distribution of the grains in the numerical body and the grinding wheel must be the same.

2.2.2.2. Domain dimensions. The volume of the *μSM* results from a compromise between computational cost and an efficient representation of the effects of stress and deformations induced by grinding and centrifugal forces. To set the limits of the domain, a 3D static stress-strain analysis was conducted using a Finite Element model. Grinding forces were applied to a rectangular region delimited by a half of contact width *w/2* and the actual contact length l_c. First, *w/2* is modelled to reduce the computational cost since the response from the other half will be identical. Then, l_c can be determined by using the classical formula (Eq. 2) by Rowe [41]) that considers the geometric contact length l_g and the Hertz deformations of the two bodies in contact:

$$l_c^2 = l_g^2 + l_f^2 = a_e d_e + \frac{8R_r^2 F_n' d_e}{\pi E^*} \tag{2}$$

Here a_e is the real depth of cut, d_e is the equivalent wheel diameter, R_r is the roughness factor (Rowe and Qi [42]), F_n' is the normal grinding force per unit width obtained from experiments, and E^* is the combined Young modulus of the grinding wheel and workpiece.

A 3D model of the grinding wheel was set up using ANSYS® Mechanical. The grinding wheel is meshed with three-dimensional hexahedron elements. The mesh size is 1 mm, which is uniform throughout the wheel except in the critical area, where it is refined to 0.5 mm. The grinding and centrifugal forces, contact area, and wheel properties used for the analysis correspond to the experimental tests described in Section 3. The model and the deformations obtained are shown in Fig. 3. Values of deformation exceeding 0.8 μm are found only in the vicinity of the contact area. Upon inspection of these results, it was decided to set the limits of the *μSM* domain at 2 times the actual contact length ($2l_c$); and

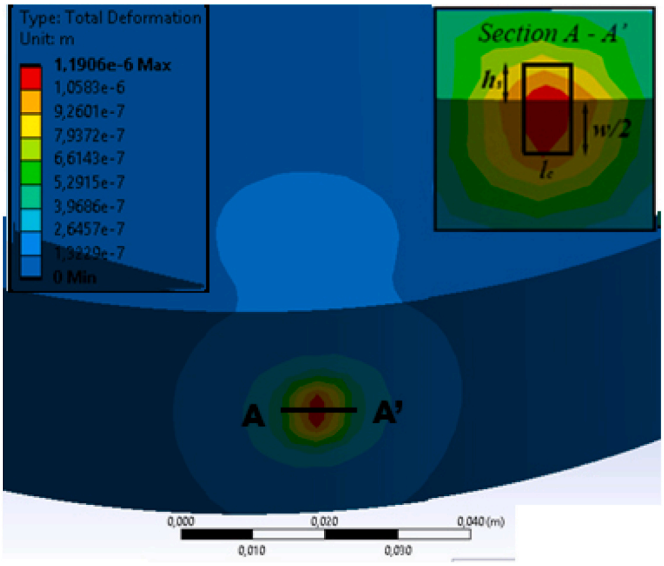

Fig. 3. FEM model of wheel deformation under the effect of grinding and centrifugal forces.

the grinding width (w). To model enough wheel material in the radial direction, a height (h_s) of 6 mm was initially fixed.

2.2.3. Calibration of mechanical properties and boundary conditions

The micro mechanical properties of the *μSM* were obtained following the procedure described by Andre et al. [38]. The micro mechanical properties (E_μ, ν_μ, r_μ and $\sigma_{f\mu}$) of the beams of the *μSM* can be calibrated through virtual tensile tests using the mechanical properties of the grinding wheel (E_s, ν_s and σ_f). The calibration process involves two steps: calibration of r_μ and calibration of E_μ and $\sigma_{f\mu}$. The influence of ν_μ on macro properties is minimal. Using 10,000 DEs is considered suitable for virtual tensile tests to ensure acceptable precision. Due to the limited impact of ν_μ on macro parameters, an arbitrary value of $\nu_\mu = 0.2$ is chosen. Through iterative adjustments in the first virtual tensile test, a stable value for ν_s is achieved, followed by fixing r_μ. In the second virtual tensile test, further iterations lead to stable values for E_s, ν_s and σ_f. Finally, E_μ and $\sigma_{f\mu}$ are fixed.

After numerical sintering, the boundary conditions of the μSM were established as follows:

- The wheel is infinitely rigid in axial, tangential and radial directions beyond the deformation region. To do so, the degrees of freedom of the DEs on the plane XY, YZ and lateral walls are restricted, as shown in Fig. 4.
- The coefficient of friction is applied to the contact between wheel and workpiece.
- Centrifugal force is applied to each DE according to the rotational speed of the grinding wheel.
- The contact law is implemented when there is contact between the DEs and workpiece . A value of contact stiffness must be calculated.
- The workpiece is modelled as a non-degradable body. It was decided to set the limits of the workpiece at the actual contact length, with half of the grinding width and an arbitrary height.

2.2.4. Fracture criterium

Volumetric wear is related to brittle fracture of bond bridges [43]. The Rankine criterium of maximum stress was implemented in GranOO workbench for the maximum failure stress of the beams. Element removal is performed when all the beams attached to the DE reach the maximum failure stress (Eq. (3))), where σ is the normal tension of the beam, τ is the tangential tension of the beam, and $\sigma_{f\mu}$ is the failure stress of the beam. The beam breaks (see Fig. 5) if it meets the following condition:

$$\sigma + \sqrt{\sigma^2 + 4\tau^2} \geq \sigma_{f\mu} \tag{3}$$

2.2.5. Contact stiffness and system of forces acting on the model

Contact stiffness for the *μSM* must be obtained from experimental values of grinding forces and from a theoretical value of grain penetration (δ_{max}). Following classical models [41], grit penetration can be determined from the expression:

$$\delta_{max} = \frac{l_c^{\,2} - a_e d_e}{4 d_e} \tag{4}$$

where, l_c is the actual contact length, a_e is the real depth of cut, and d_e is the equivalent wheel diameter. In this approach, δ_{max} represents the maximum penetration between wheel and workpiece (see Fig. 6).

It is clear from Fig. 6 that penetration varies along the actual contact length. An average value of grit penetration (δ_{av}) can therefore be obtained using Eq. (5):

$$\delta_{av} = \frac{1}{\theta} \int_0^{\theta} [R - L_r]\, d\theta \tag{5}$$

The value of the contact stiffness can then be established using the normal grinding force F_n obtained from experiments:

$$K = \frac{F_n}{\delta_{av}} \tag{6}$$

As the workpiece acts on the *μSM*, the sum of the individual forces on each DE thus replicates the usual grinding force acting on the wheel (see Fig. 7):

$$F_n = K \bullet \sum \delta_j \tag{7}$$

The sliding speed used in the study is 30 m/s, which serves as an input for the model. To incorporate this, a simplification based on Coulomb's Law [44] is implemented in the *μSM*. Due to the high sliding speed of the tests conducted, the static friction coefficient does not significantly impact the contact. As a result, a constant dynamic friction coefficient is assumed throughout the entire contact period. This coefficient is applied to each DE in contact with the workpiece, with the aim of achieving an optimal representation of the sliding speed.

Finally, centrifugal forces are imposed on each element of the *μSM*:

$$f_{cj} = m_j \bullet \omega^2 \bullet r_j \tag{8}$$

where m_j *is* the mass of each DE, r_j is the distance from the center of each DE to the center of the wheel, and ω is the rotational speed of the grinding wheel.

2.3. RμSM (randomization of the μSM)

As explained previously, the *μSM* alone is unable to completely explain the wear behavior of the grinding wheel. Together with mechanical properties, the stochastic nature of the location of the grains and the bonding bridges critically impacts the phenomenon of bond fracture. Therefore, any explanation of volumetric wear must account for the interaction between these two factors.

The *RμSM* was created using the same assumptions about wheel

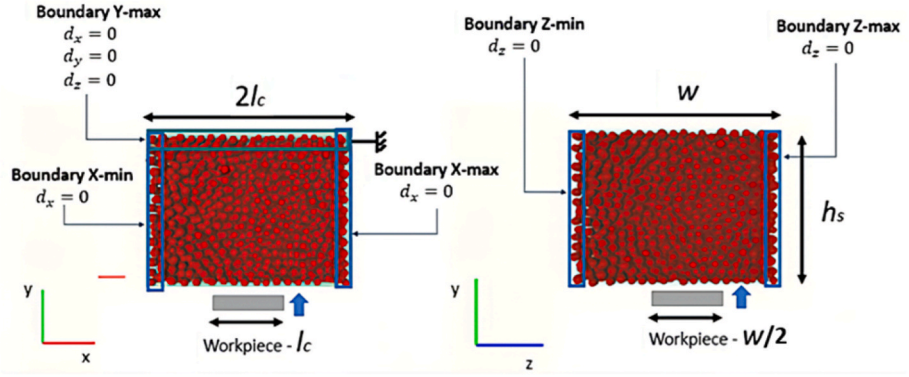

Fig. 4. Boundary conditions imposed on the μSM.

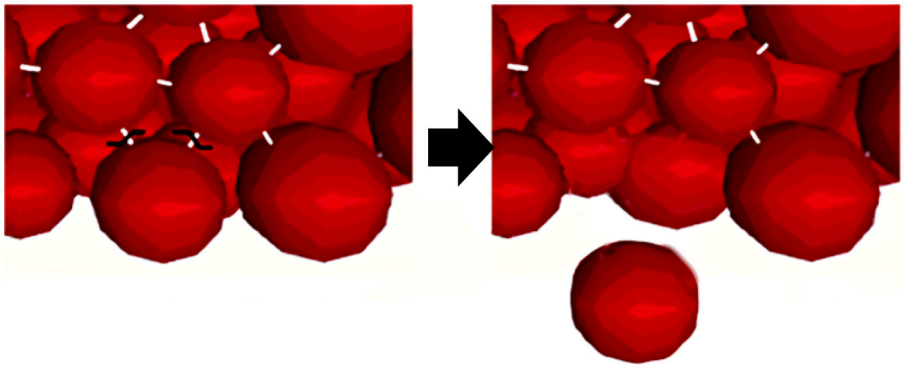

Fig. 5. DE removal from the *μSM* following Rankine criterium.

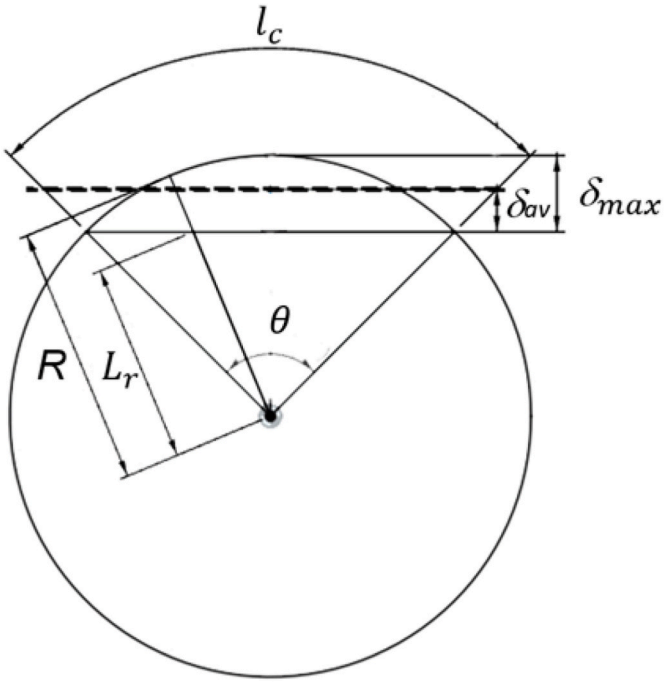

Fig. 6. Schematic diagram for calculation of δ_{av}.

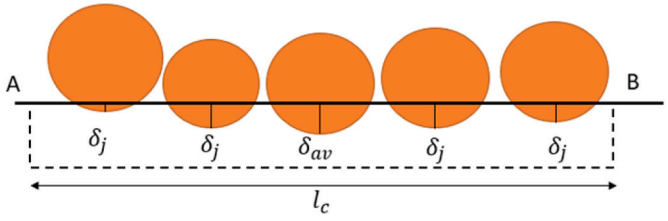

Fig. 7. Actual grit penetration δ_j in the μSM.

density and grain size/distribution already explained in Section 2.2.2. The numerical sintering method already used for the *μSM* [38] was then applied to the complete domain of the grinding wheel (see Fig. 8). The result was a normal distribution with similar characteristics to the *μSM* (average grain diameter d_g 0.360 mm, see Table 1). Therefore, the actual location and radius of each DE are available in the *RμSM*.

The *RμSM* also allows for representing a rotation counter for the wheel, thus providing the time scale required to measure the grinding ratio *G*. During simulation, the outermost grain (i.e., DE) of the wheel is located in the *RμSM*. Its distance to the center of the wheel is R_i, where *i*

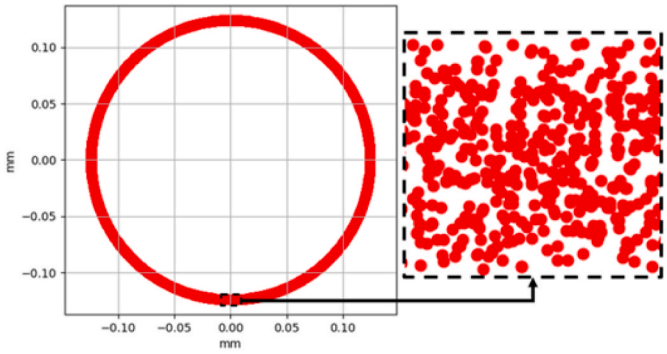

Fig. 8. RμSM (randomization of the μSM) sintered in the complete domain of the grinding wheel.

Table 1
Comparison of parameters between *RμSM* and real wheel.

	RμSM	Real	
Grain density	16.78	16.84	grains/mm^3
Mean radius	0.18	0.18	mm
max radius	0.259	0.259	mm
min radius	0.124	0.124	mm

is the counter for the number of rotations of the wheel. The outermost grain represents the first contact between wheel and workpiece .

2.4. Active grain density

In order to integrate the *μSM* and *RμSM*, it is crucial that the surfaces of both are equal without any excess or defective protruding grains. Discrepancies between actual and numerical active grain densities are often caused by the effects of element pile up during numerical sintering (already described by Osa et al. [34]) or because of a lower active grain density at the boundaries of the *RμSM*. The grain density was measured throughout both the *μSM* and the *RμSM*, and the results are displayed in Fig. 9.

In the case of the *μSM*, in the first mm from the point of contact with the workpiece, the surface grain density was 17.32 grains/mm^3, which subsequently fell to an almost constant value (with slight fluctuations) with an average value of 16.36 grains/mm^3. On the upper boundary of the model, element pile up appears again, increasing grain density to over 17.5 DE's/mm^3. For the *RμSM* the density of the first 0.5 mm layer was very low (3.33 grains/mm^3), after which a constant value of 16.78 grains/mm^3 was reached.

Inspection of grain density in the actual grinding wheel suggests that this value is conditioned by the dressing process. In fact, dressing affects

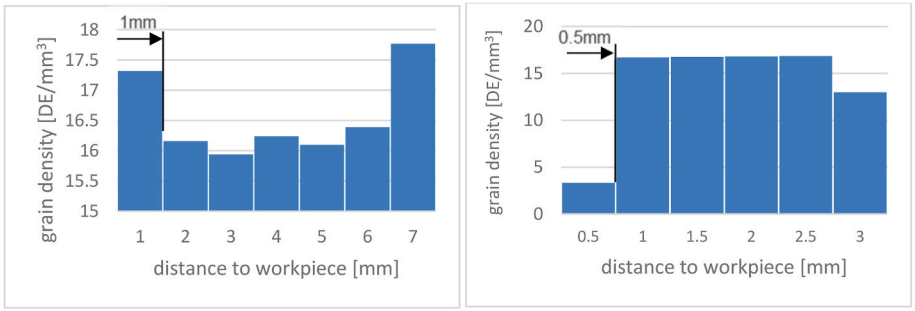

a. b.

Fig. 9. Surface grain density throughout both μSM and RμSM. a) Effect of element pile up produced by numerical sintering; b) lower density on the boundary of the RμSM.

wheel performance (see experimental results in Fig. 14). Therefore, as a preliminary approach, it was decided that the *μSM and RμSM* would be used to simulate the actual average structure of the grinding wheel, with no consideration of the dressed region. Taking this into account, the average grain density of the wheel is 16.84 grains/mm^3. As a consequence, coherence between numerical models and the actual grinding wheel requires that the layers of the models affected by element pile up (*μSM*) and low density (*RμSM*) are removed. After removing those layers, the resulting structures are shown in Table 2 for comparison.

2.5. Integration of μSM – RμSM and estimation of wheel wear

The flow chart in Fig. 10 represents the integration of the *μSM* and *RμSM*. The movement of the workpiece was applied to the *μSM*, which had previously been calibrated using the experimental data obtained in Section 3. Through the actual contact stiffness, the actual (as measured experimentally) normal and tangential forces were applied to the *μSM*. The effect of centrifugal forces was also included. Stress and deformation fields were then obtained by solving the DEM model, which in turn allowed for calculating the number of DEs (that is, abrasive grains) lost (N_r) and critical penetration (δ_C). δ_C refers to the depth of penetration that leads to the initial separation of at least one discrete element of the *μSM*. Moreover, the normal (F_n') and tangential grinding force per unit width (F_t') and the number of DEs in contact were confirmed before exploring the complete surface of the *RμSM*. The reference was set at the outermost DE (grain). The elements that lie within the penetration δ_C, were used as the reference to locate the adjacent elements that must be removed. For each reference DE, a number of adjacent elements equal to that calculated by the *μSM* were removed, and a new rotation began (i=i+1). The new outermost grain was then used as a new reference and the procedure repeated. The distance between the current outermost grain and that of the previous rotation (in other words, the radial wear (Δ)) was measured before examining the *μSM* again. From the workpiece position previously left, Δ was applied. If the wheel breaks, a new number of DEs removed ($N_{r\ new}$) and new critical penetration ($\delta_{C\ new}$) are established. Moreover, the new normal ($F_{n\ new}$'), new tangential grinding force per unit width ($F_{t\ new}$'), and the new number of DEs contact are checked. Otherwise, N_r and δ_C are maintained. Finally, the *RμSM* is explored, and the procedure is repeated.

The procedure finishes when the maximum established workpiece displacement has been reached. The *μSM* is highly sensitive to the position of the grains, which is why a sufficient number of iterations is required to minimize uncertainty in the calculation of the *G* ratio.

Table 2
Structural comparison of *μSM*, *RμSM*, and the actual grinding wheel.

	μSM	*RμSM*	Actual grinding wheel
Grain density (grains/mm^3)	16.36	16.78	16.84
Density (g/mm^3)	1.776e^{-03}	–	1.776e^{-03}
Mean radius (mm)	0.18	0.18	0.18
Max radius (mm)	0.24	0.259	0.259
Min radius (mm)	0.122	0.124	0.124

3. Experimental grinding tests

Experimental tests involve measuring wheel wear evolution during grinding under industrial conditions. Grinding experiments were conducted on a three-axis CNC surface grinder Blohm Orbit 36. The coolant used was a 5% water-based oil emulsion. The specification of the vitrified monocrystalline alumina wheels was MA46EF12V, with dimensions of ∅250x127 × 40 mm. Abrasive grits were 100% cubic monocrystalline alumina. A very soft wheel was chosen with the aim of promoting volumetric wear. An AISI 02 hardened tool steel T-profile block, hardness 54HRc was used as workpiece material. Grinding conditions and wheel characteristics are displayed in Table 3. During the tests, power consumption was measured using a Load Controls Universal Power Cell, Model UPC-FR, together with a data acquisition card NI usb-6008. Further, normal and tangential forces (F_n, F_t) were recorded using a Kistler 9257B dynamometer. The procedure used to measure the wheel volumetric wear is shown in Fig. 11. Additionally, the real material removal quantity was measured during the grinding tests using a millesimal dial gauge. Subsequently, the wheel profile is captured using a Dino-Lite Microscope, and the profile processing is performed using Matlab.

The grinding forces and power consumption were measured at each grinding pass. In order to measure the wheel wear and real materials removal rates, the overall experimental test was divided into 11 blocks. Table 3 details number of passes of each block. After each block, the part material removed, and the wheel profile wear were measured.

Fig. 12 shows the evolution of specific power (P') and specific grinding energy (e_c) compared with specific material removal. The graph can clearly be divided into two regions. The first zone is dominated by the dressing operation (until V_w' = 400 mm^3/mm), where P' *and* e_c reach a maximum value of 0.21 kW/mm and 23.21 J/mm^3 respectively while the second zone is unaffected by the dressing operation, in which the values of P' and e_c remain almost constant (0.18 kW/mm and 19.92 J/mm^3 respectively). It is clear that once the effect of the dressing process disappears, the values of P' and e_c decline. Considering that the overlap ratio used in the dressing process was 7.33 (fine dressing), this behavior is coherent with the basic grinding theory. Additionally, in this second part, the constant value of P' and e_c means that the abrasive surface has similar cutting edges every time, so the predominant type of wear must be grain fracture and bond fracture. These results suggest that attritious wear is not expected to appear. Rather, volumetric wear is more likely to occur, which is reasonable given that the grinding wheel is very soft.

Fig. 13 shows the evolution of the normal and tangential components of the specific grinding force (F_n', F_t' respectively) versus accumulated

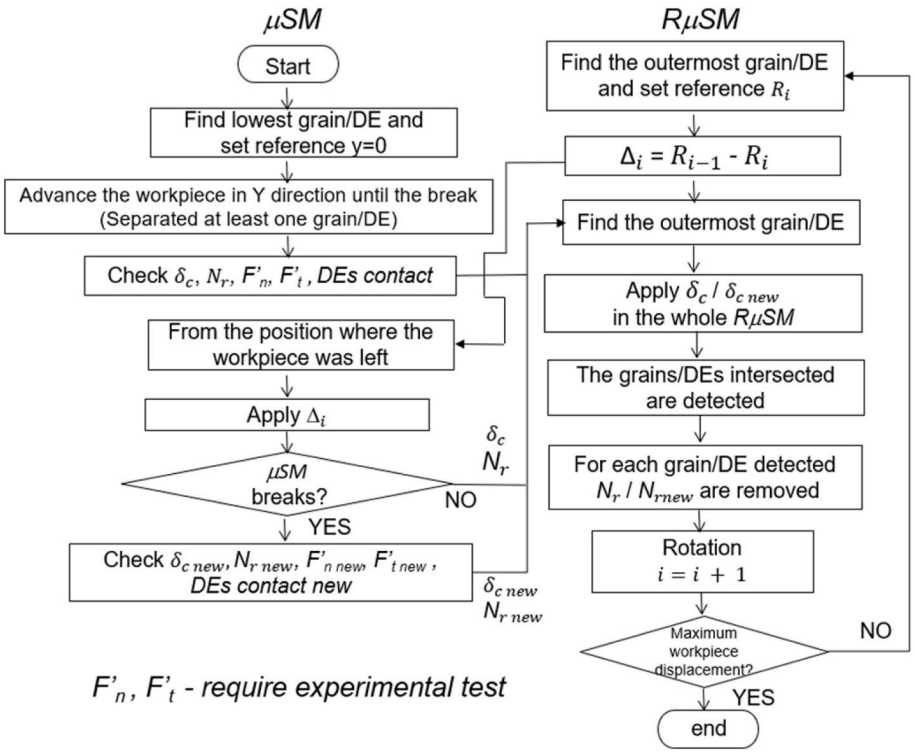

Fig. 10. Flow chart showing integration of the microscale model (μSM) and the randomization of the μSM (RμSM).

specific material removal. This pattern of results appears to be similar to the power results, revealing the presence of two regions. The tangential force can be related to the power consumption using Eq. (9)):

$$P = F_t \bullet v_s \tag{9}$$

According to this equation, in the dressing transitional zone a maximum specific power consumption value of 0.24 kW/mm is reached, while in the non-affected stationary dressing zone, a mean value of 0.18 kW/mm is observed. These results are coherent with respect to the obtained P' shown in the previous graph. Regarding the specific normal force, this remains constant in the non-affected stationary dressing zone (F_n' and F_t' show average values of 16.39 and 6.12 N/mm respectively). Additionally, the force ratio remains practically constant across the entire test ($F_t'/F_n' \approx 0.37$). This observation confirms that the surface grinding wheel maintained a consistent material removal capacity throughout the experiment, thus minimizing the occurrence of attritious wear and maximizing volumetric wear. Finally, the standard deviation of the measurements for both components remained at 15% throughout the entire test.

The evolution of volumetric wear and G ratio are plotted in Fig. 14. Upon inspection of this graph, the above finding from the force analysis becomes even more evident. The two regions already described can be clearly identified: the first region until approximately $V'_w = 350$ mm^3/mm corresponding to the assumed influence of the dressing operation, and a second region in which the effect of the actual structure of the grinding wheel is dominant. It can be observed that evolution of volumetric wear shows linear behavior in both regions, which is compatible with the existing literature. R^2 values are 0.989 in the first region, and 0.998 in the second. From these plots, the G ratio can be found for both lines. Values of G ratio are 2.22 for the first region and 1.09 for the second. The results revealed very low G ratio values, which are expected, given the selection of a very soft wheel for the experiments. Given that the transitional effects of the dressing process will not be considered in the numerical modelling of the grinding process, the G ratio of the second region will be used for model validation since this is not affected by the dressing process.

4. Multiscale simulations and discussion of results

4.1. Calibration of the μSM

4.1.1. Mechanical properties of the beams

The mechanical properties of the beams of the *μSM* were obtained using the methodology proposed by André et al. [38]. Virtual tensile tests were conducted by varying the mechanical properties of the beams, thus ensuring that the macro mechanical properties of the numerical sample are equal to those of the actual material of the grinding wheel. Therefore, the first step involved characterizing the properties (E_s, υ_s and σ_f) of the composite material of the grinding wheel. The elastic modulus of the wheel, E_s, was determined using the Grindosonic measurement technique [45]. Additionally, the Poisson ratio (υ_s) was calculated from the obtained E_s using the classic elastic modulus formula [45]. To determine the failure stress σ_f in accordance with ASTM standard C 1161, three-point bending tests were conducted on three samples (span length: 120 mm; loading rate: 2 mm/s). The bending strength of the samples was calculated through the force applied using a common equation provided in the standard literature. The results are plotted in Fig. 15. The failure stress σ_f was established by calculating the average value of the maximum strength of the 3 specimens. Finally, the mechanical properties used for calibration are displayed in Table 4.

It can be observed that the deviation is very small for the value of the failure stress. Results of 23.66 MPa (sample 1), 20.51 MPa (sample 2) and 21.02 MPa (sample 3) have been measured during the tests. The average value is 21.73 MPa and the standard deviation is 1.68 MPa. In fact, the largest discrepancy among the three tests is concentrated at the beginning of each test. Specifically, when applying the load in the three-point bending test, it becomes challenging to accurately measure the exact moment when the specimen starts to deform.

4.1.2. Actual contact length, contact stiffness, and friction coefficient

The theoretical basis for determining the actual contact length, contact stiffness, and the friction coefficient is shown in Equation (2)), 6) and 10) respectively. The experimental data collected in Section 3 were

Table 3
Test conditions.

Grinding wheel			
Dimensions (mm)		∅250x127 × 40 mm	
Specification		MA46EF12V489P20P	
Abrasive volume fraction, V_g (%)		41	
Porosity volume V_p (%)		47.3	
Average grain diameter, d_g (mm)		0.36	
Maximum grain diameter d_{gmax} (mm)		0.518	
Minimum grain diameter d_{gmin} (mm)		0.248	
Mass m (Kg)		2.5	
Density ρ (Kg/m^3)		1776	
Cutting speed v_s (m/s)		30	
Workpiece material			
Material		AISI 02 (90MnCrV8)	
Hardness (HRc)		54	
Dimensions (mm)		30x10 × 125 mm	
Grinding conditions			
	a_e = 0.036 mm	v_s = 30 m/s	v_w = 0.25 m/s
	Q_w' = 12.5 mm^3/mm·s	q_s = 120	
Dressing conditions			
	a_{ed} = 0.010 mm	V_d = 250 mm/min	v_s = 30 m/s
		U_d = 7.33	
Number of passes	*10*	*20*	*40*
Grinding test block	*1–4*	*5–8*	*9–11*
Force measurements			
Dynamometer plate: Kistler 9257B		Acquisition rate 10000 Hz force range ±500 N Low Pass filter Cut-off frequency: 0.25	
Power measurements			
Wattmeter Load Controls Universal Power Cell: Model UPC-FR		Acquisition rate 10000 Hz Low Pass filter Cut off frequency: 0.25	

used to determine the numerical values for the above variables (see Table 5). In addition, the roughness factor (R_r) was considered. This parameter accounts for the influence of several variables, such as the roughness of the grinding wheel, dressing condition, and workpiece properties. According to the literature, R_r typically ranges from 5 to 15, depending on the specific combination of these factors. Osa et al. [34] proposed a static model that simulates the contact between the grinding wheel and workpiece and found that R_r is 5.1 under similar dressing conditions to those studied in this work. Moreover, as the forces are derived from experimental tests, it was possible to determine the coefficient of friction by employing Eq. (10)).

$$\mu = \frac{F_t'}{F_n'} \tag{10}$$

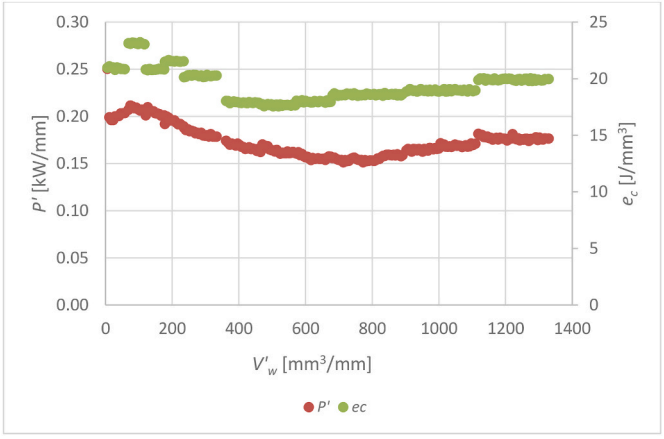

Fig. 12. Specific power (P') and specific grinding energy (e_c) vs. specific volume of part material removed (V'$_w$).

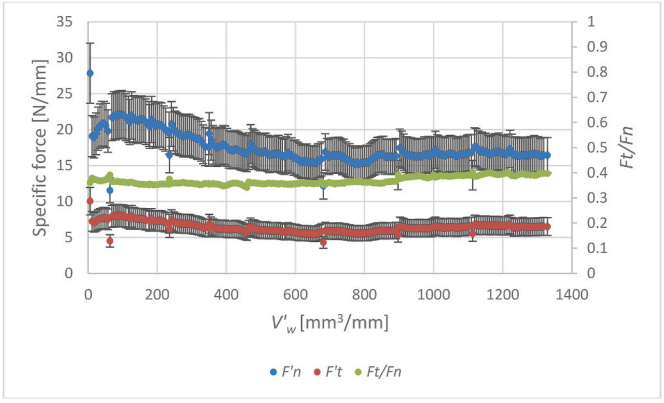

Fig. 13. Specific normal (F'$_n$) and tangential (F'$_t$) grinding force vs. specific volume of part material removed (V'$_w$).

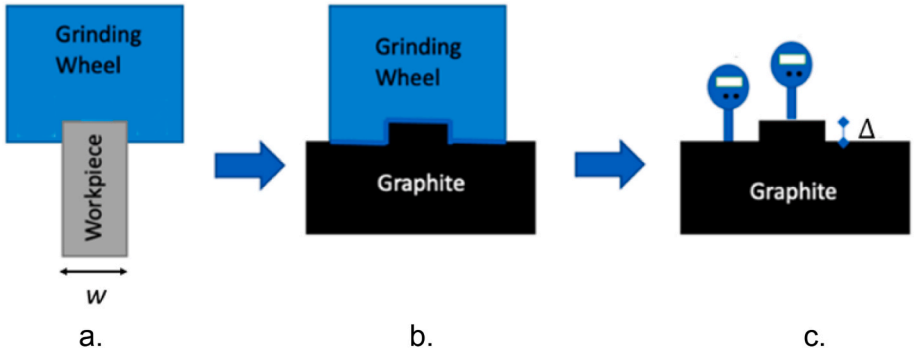

Fig. 11. Procedure for measuring radial wear of the grinding wheel. a) grinding operation, b) passing the griding wheel over the graphite, c) measuring the radial wear with a dial gauge.

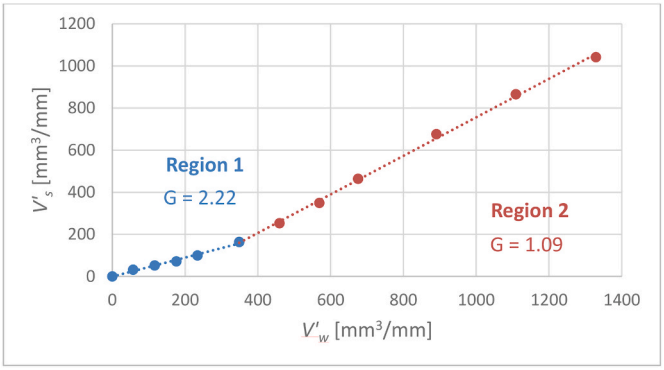

Fig. 14. Specific volumetric wear V'$_s$ versus specific metal removed V'$_w$.

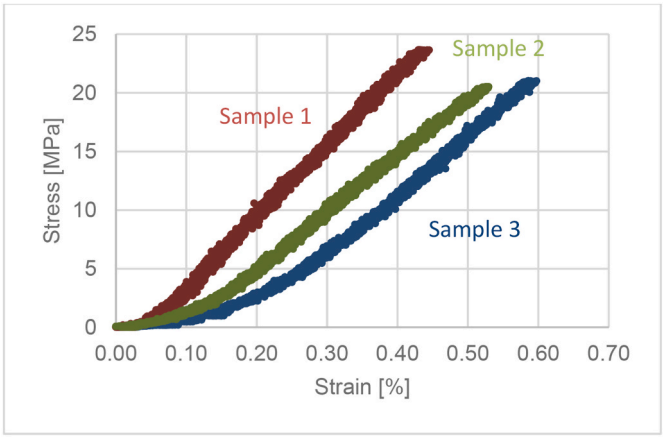

Fig. 15. Results of the three-point bending tests on three samples of the wheel material.

Table 4
Calibration of the μSM.

Young's modulus of the grinding wheel E_s (GPa)	20
Failure stress of the grinding wheel σ_f (MPa)	21.75
Young's modulus of beams E_μ (GPa)	120
Failure stress of beams $\sigma_{f\mu}$ (MPa)	167
Poisson ratio υ_s, υ_μ	0.2
Beam diameter ratio r_μ	0.57

Table 5
Actual contact length, contact stiffness and friction coefficient.

Real depth of cut a_e (mm)	0.036
Grinding wheel diameter d_e (mm)	250
Roughness parameter R_r	5.1
Normal force per unit width, F_n' (N/mm)	16.39
Tangential force per unit width, F_t' (N/mm)	6.12
Combined Young Modulus E^* (GPa)	19.08
Average value of grit penetration δ_{av} (mm)	0.00774
Actual contact length l_c (mm)	4.82
Contact stiffness K (N/m)	10632785.27
Friction coefficient μ	0.37

4.2. Variability of critical penetration and number of DEs removed in different μSMs

δ_C refers to the depth of penetration that leads to the initial separation of at least one discrete element of the wheel. To better understand the range of critical penetration and its underlying causes, a study of the variability of δ_C was carried out. To this end, 3 *μSMs* (pre-processing 1, 2, 3) were created using procedure 2.2. This approach generates models with different positions of the discrete elements that closely resemble the reality of the grains on the grinding wheel. Once the models were created, the simulation was continued. Since in this case, the analysis was conducted solely on the *μSM*, the workpiece was displaced without stopping between the point of contact at the farthest grain to the maximum radial wear (determined experimentally). Once the simulation was complete, the results were analyzed. The contact generates stresses in the beams. Due to the failure criterion, the grains separate at a certain penetration, based on the configuration of their position. A summary of the results of these simulations is shown in Fig. 16. It is clear that the different grain positions in contact with the workpiece provide different values of δ_C and N_r.

In each *μSM*, the N_r for a δ_C is determined by measuring the movement of the workpiece from the time it touches the grain until at least one grain is separated from the *μSM*. As shown in Fig. 16, the pattern of results is similar for the three *μSMs*. The calculations indicate that the mean for δ_C is 0.00685 ± 0.0262 mm (mean ± variance), and the mean for N_r is 4.28 ± 16.1. It should be noted that negative values do not make physical sense in this context. A correlation analysis was also conducted to investigate the association between δ_C and N_r, yielding a covariance between the two variables of 0.0101. This indicates the linear relationship between the variables, and a positive covariance suggests that both variables increase together.

Given their significance, it was necessary to analyze the above results in greater detail. The resistance of bonding bridges to bond fracture is conditioned by the geometrical arrangement of the grains, so that δ_C becomes a measure of this resistance. Obviously, the maximum penetration to which a grain can be subjected is δ_{max} (see Section 2.2.5), and in this case, its value is 0.01429 mm. From a mechanical strength perspective, some grain configurations can withstand penetrations greater than δ_{max} (9.56% of the values in Fig. 16 are above that value). In other words, for a given δ_{max}, as many as 90.44% of the grain configurations can result in detachment of grains from the vitreous bonds. In practice, the combination of operating parameters and elasticity of the grinding wheel and workpiece sets the maximum possible penetration δ_{max}. Therefore, the simulations are truncated at this maximum value. Fig. 16 also provides compact and useful information about the influence of grinding parameters on actual performance in terms of hardness of the grinding wheel. It is widely accepted in industry that "*for a given wheel, hardness performance is dependent on grinding parameters*". However, to the best of our knowledge, this is the first attempt to numerically quantify this effect.

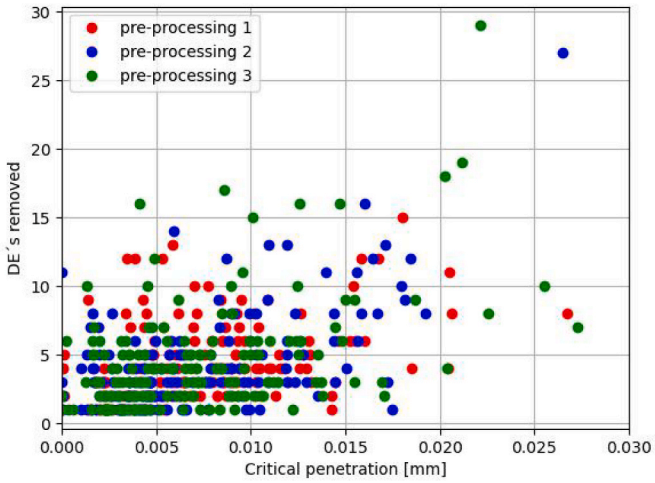

Fig. 16. Critical penetration vs DEs removed.

4.3. Validation of the system of forces acting on the μSM

The system of forces plays a crucial role in wear analysis, particularly in understanding volumetric wear mechanisms. This study is focused on analyzing the grinding forces transmitted by the bond in the wheel and validating their loads. To obtain the forces, three *μSMs* were modelled, following the same procedure as outlined in Section 4.2. Upon completing the simulations, the results were analyzed, and the specific forces (i.e., specific normal and tangential forces) and grain loss versus workpiece position are presented in Fig. 17. The data clearly indicate that when the workpiece initially compressed the *μSM*, it generated specific normal forces that could reach up to 34 N/mm. This high force was due to the presence of all grains on the surface of the model. However, as the workpiece progressed and compressed further, many grains were dislodged from the surface, creating voids, as depicted in Fig. 18. From a workpiece position of 0.15 mm, the rate of grain loss appears to be linear, indicating a constant level of wear on the surface that persists until the end of the simulation. In turn, the forces were reduced, peaking at 22 N/mm and lower. Additionally, the curve shows several sudden drops, indicating that at that instant, the workpiece was no longer in contact with the *μSM*. Overall, the results indicate that almost 600 grains were lost from the *μSM* in a workpiece displacement of 1.4 mm.

After obtaining the *μSM* results, the force peaks were extracted to facilitate further analysis, as shown in Fig. 19, which plots these force peaks at specific workpiece positions. In the steady state, the maximum specific normal force found is 22.62 N/mm at 0.51 mm workpiece position. Conversely, the specific normal force is relatively low at other workpiece positions, such as 0.43 mm and 1.12 mm, with values of 1.2 N/mm.

Finally, as mentioned previously, to conduct the validation, the experimental results of the second region need to be considered. In other words, the influence of dressing will not be considered in this first approach. For this reason, the experimental results of the specific normal force (experimental range between 13 and 20 N/mm) were compared to the *μSM* results (pre-processing 1, 2, 3) in the steady state, with the former shown in the gray zone. The validation analysis revealed that 16.96% of the specific normal force of the model fell within the experimental range. However, forces outside the experimental range were also observed to a greater extent. In particular, 13% of forces surpassed the experimental range, while a greater percentage fell below the experimental range. While these findings could be due to the fact that low forces are generated in some sections of the wheel in contact, there will also be a degree of overlap with the high forces generated on other sections of the wheel, which will be detectable during the measurement process.

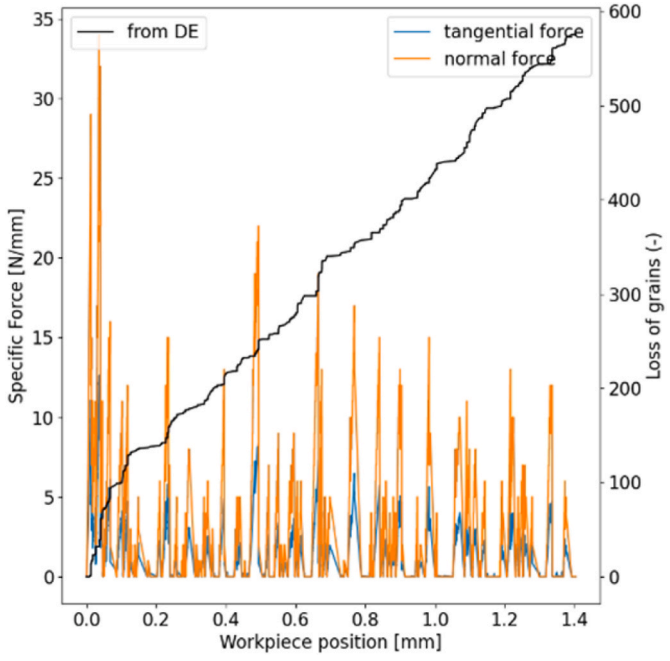

Fig. 17. Measurement of specific forces and grain losses according to workpiece position in *μSM*.

To understand volumetric wear, the loads generated by forces were analyzed. In terms of the maximum failure stress, $\sigma_{fu} = 167$ MPa corresponds to beam failure according to the imposed failure criteria. The figure illustrates the evolution of stresses in the beams at two different contact positions. It appears that the grinding force propagates through the DE-beam and its neighboring beams. During compression, green, yellow, and red colors (corresponding to 50 MPa, 80 MPa, and 167 MPa, respectively) appear, as shown in Fig. 20. As observed, four grains above the contact grain were affected by stresses of 50 MPa in the beams, and three grains above were affected by the maximum stress, which could be taken to indicate the presence of residual voids on the wheel surface and a high rate of grain removal, as evidenced in Section 4.2.

Based on the validation results, it can be concluded that the *μSM* forces are able to accurately simulate the mechanical behavior and grinding performance at a single contact length. Therefore, the information obtained from *μSM* is considered reliable for determining radial wear and G-ratio of the whole grinding wheel.

4.4. Multiscale simulations: validation of the predictions of radial wear and G ratio

This section presents the validation of radial wear and *G* ratio predictions obtained through multiscale simulations. For this purpose, a comparative study was conducted on the results of the simulations and the experimental data presented in Section 3. To obtain the *G* ratio it is necessary to calculate the specific volumetric wear of the grinding wheel (V_s') and the specific volumetric material removal of the workpiece (V_w'). In the simulations, Vs' can be obtained from radial wear measured in the *RμSM*, while V_w' can be calculated using the number of rotations in the *RμSM*.

The assumption that the grains are perfectly spherical *DEs* adds an additional uncertainty with respect to the actual critical penetration δ_C. This was already explained in section 2.2.2. To account for this effect, a shape factor S_f was introduced, which is expressed as the percentage deviation of the critical penetration δ_C with respect to the value obtained from the *μSM*. A sensitivity analysis of the model was conducted in which S_f was varied from 0% to 10% with respect to the critical penetration (see Fig. 21).

Fig. 22 presents the comparison between experiments and simulations including the sensitivity analysis of the shape factor S_f. As already stated in previous sections, in this preliminary step, the model simulates the behavior of the wheel in *region 2*, this is, with no consideration for *region 1* (see Fig. 14). The region in the experimental curve affected by dressing clearly shows a very different behavior. Modelling of the as-dressed region will be investigated in future research. Therefore, the current comparison was limited to the steady-state region in which the grain density is similar (see Table 1).

The results reveal a high degree of concordance between experiments and multiscale simulations. The best fit corresponds to a value of S_f of 6%. In this case, both simulation and experimental results show a *G* ratio of 1.09. In terms of δ_C, a shape factor of 6% represents a maximum deviation in the critical penetration of less than 1 μm (specifically 0.8574 μm), which would be expected given the effect of the presence of micro-cutting edges on the abrasive grits. In terms of radial wear, multiscale simulation also produces very solid results, as shown in Fig. 22. The local effects on grain detachment are very well represented by the multiscale simulation model, while the accumulated radial wear accurately represents the volumetric wear behavior of the grinding wheel.

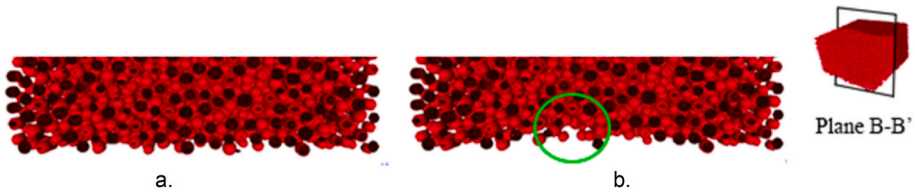

Fig. 18. Voids left on the surface by the volumetric wear seen in the cut plane B-B' of μSM. a) Workpiece position 0.2 mm b) Workpiece position 0.25 mm.

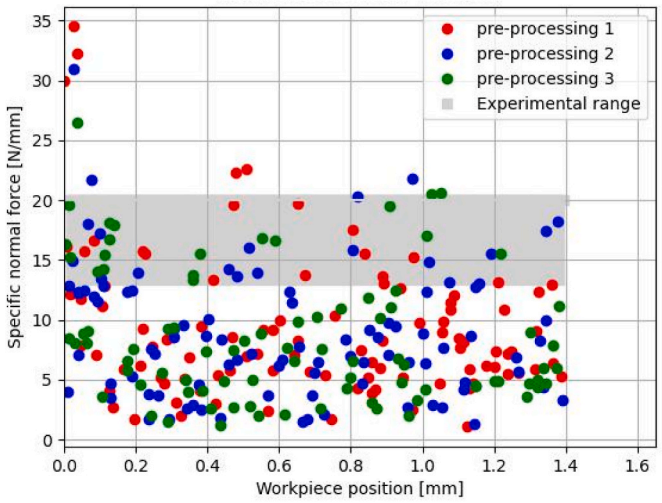

Fig. 19. Extracted peaks of the specific normal force according to workpiece position.

Fig. 23 illustrates the actual profile of the grinding wheel and the simulated profiles of the *RμSM* for each grinding test block. The actual morphologies of the grinding wheel wear are obtained from the graphite cube shape. For the comparative analysis, the profiles of test blocks 7, 9, and 11 are considered, representing region 2. To ensure a consistent contact width between the *RμSM* and experimental tests, a wear width of 5 mm is applied. The *RμSM* profile is obtained when the number of wheel revolutions matched the experimental test upon completing the grinding test block. It can be observed that the *RμSM* profiles accurately reproduce the level of radial wear observed in the profiles of the grinding wheel. The shape of the *RμSM* profile tends to be linear along the wheel width. This comprehensive approach provides a strong prediction of the *RμSM* profile that closely matches the actual profile of the grinding wheel.

The discrepancy in region 1 becomes obvious when analyzing the results. As already explained, the role of grain density on the overall system is critical. Since the density of the dressed region is different to that of the rest of the body of the wheel, the results are also very different. Moreover, the dressing-induced damage of the vitreous bonding bridges cannot be discarded as an additional source of uncertainty. These effects will be examined in future research since dressing plays a fundamental role in industrial grinding operations. Nonetheless, and based on the validation results, it can be concluded that the proposed multiscale simulation approach provides, for the first time, an effective tool for understanding the mechanisms of volumetric wear of grinding wheels by considering mechanical properties of the wheel, process parameters, and the stochastic nature of the location of abrasive grains.

5. Conclusions

A comprehensive approach to understanding the phenomenon of volumetric wear in grinding wheels has been presented for the first time.

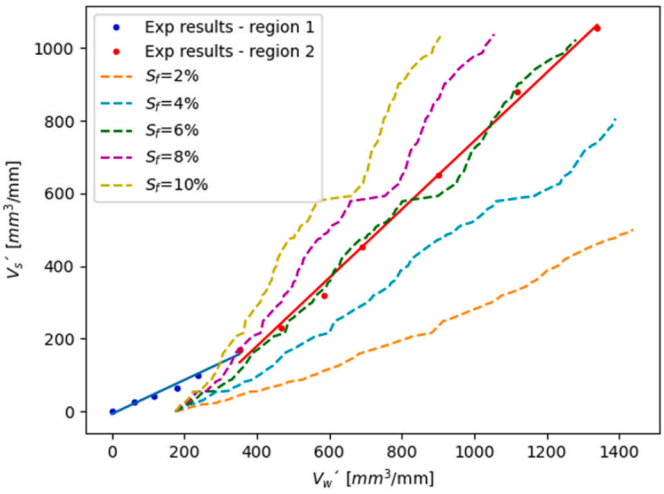

Fig. 21. Comparison of wear between multiscale simulations and experiments.

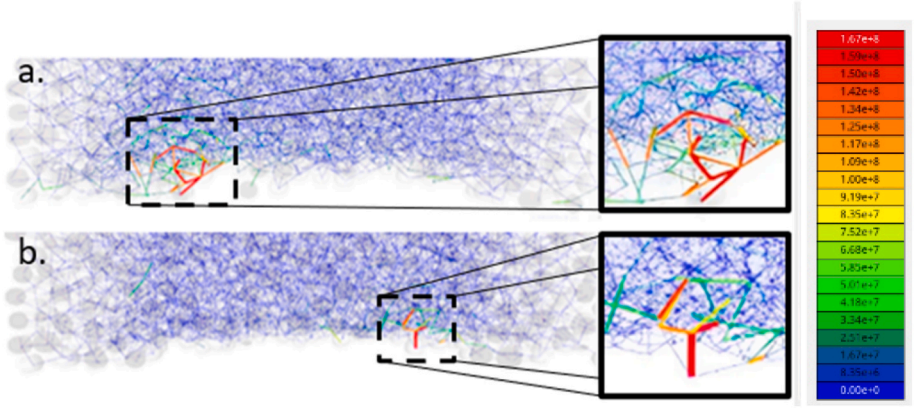

Fig. 20. Beam stress observed in the cut plane B-B' of μSM. [Pa]. a) Workpiece position 0.36 mm. b) Workpiece position 1.05 mm.

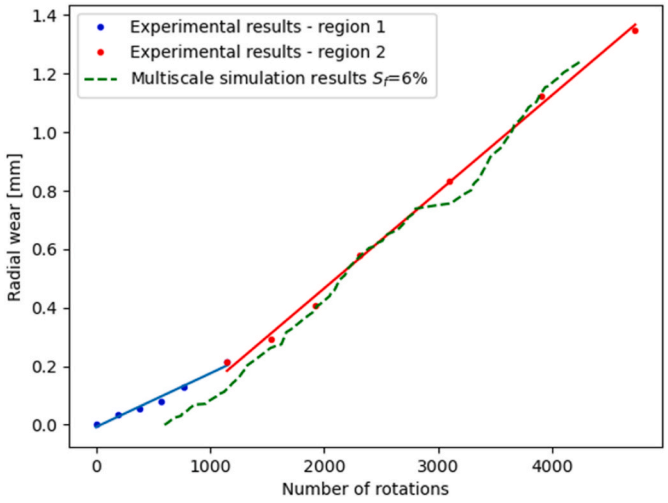

Fig. 22. Experimentally measured and simulated radial wear for a shape factor value of $S_f = 6\%$.

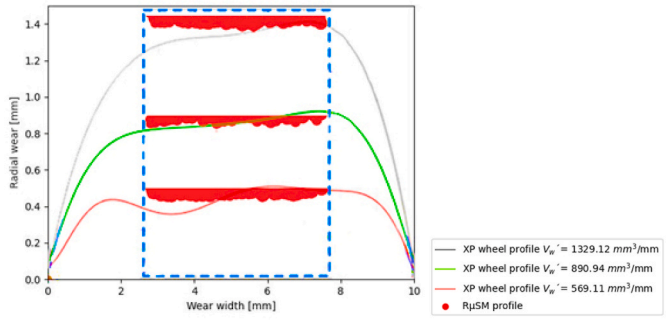

Fig. 23. Evolution of the graphite replica profile (XP, experimental) and simulated *RμSM* profile at three different values of V'_w.

This approach considers the mechanical properties of the wheel, the effect of grinding parameters, and the random location of the abrasive grains. On the basis of the work presented here, the following conclusions can be drawn:

- The fields of stress and deformation within the grinding wheel can be determined by using a DEM model that represents the mechanical properties of the wheel and its structure under the effect of process forces (grinding and centrifugal). By simulating only the equivalent of a given contact length, simulation time can be drastically reduced. However, this is not enough to simulate volumetric wear since it does not account for the random location of grains on the entire wheel. Alternatively, combining the DEM model with a geometrical representation of the location of the grains provides a complete characterization of the wheel at low computational cost.
- A statistical distribution of the critical penetration values that produce detachment of groups of abrasive grains has been successfully obtained using the *μSM*. In the case studied, for a theoretical maximum penetration of 0.01429 mm, as much as 90.44% of the possible grain arrangements can be pulled out from the wheel under the effect of grinding and centrifugal forces. By reducing the theoretical maximum penetration, this high *potential wear* can be drastically reduced, and this effect can be quantified. To the best of our knowledge, this is the first attempt to numerically quantify the influence of grinding parameters on actual grinding wheel performance in term of hardness.
- The experimental results of the specific normal force were compared to the *μSM* results. This validation analysis revealed that 16.96% of the specific normal force of the model fell within the experimental range. However, a larger proportion of forces fell outside the experimental range, with 13% exceeding the experimental range and a higher percentage falling below this range. Although these findings could be due to the fact that low forces are generated in some sections of the wheel in contact, these would overlap with the higher forces generated in other sections of the wheel, which would be detectable during measurement.
- The assumption that the grains are perfectly spherical *DE*s adds an additional uncertainty with respect to the actual critical penetration δ_C. To account for this effect, a shape factor S_f has been introduced which is expressed as the percentage deviation of the critical penetration δ_C. Results of radial wear and grinding ratio show a very good degree of agreement between experiments and simulations. The best fit corresponds to a value of S_f of 6%. In this case, both simulation and experimental results show a G ratio of 1.09. In terms of δ_C, a shape factor of 6% represents a maximum deviation in the critical penetration of less than 1 μm (specifically 0.8574 μm), which would be expected given the effect of micro-cutting edges on the abrasive grits. Accumulated radial wear is also successfully represented by the multiscale approach.
- The effect of dressing has not been considered at this stage of the research. Although the multiscale approach presented contains most of the information required, in the case of dressing there is a need to further analyze the influence of dressing parameters on surface grain density, along with the possible damage to the mechanical strength of the bonding bridges caused by the dressing operation. These issues will be explored in future research.
- From the point of view of the authors, the most relevant scientific advancement is the development of a theoretical framework to explain and predict volumetric wear of vitreous bond alumina grinding wheels. This is relevant achievement taking into account that to the best knowledge of the authors, this is the first attempt to theoretically predict volumetric wear.

CRediT author statement

Pazmiño Tyrone: Formal analysis, Writing- Reviewing and Editing. **Pombo Iñigo.**: Project administration, Resources, Validation. **Girardot Jérémie**: Software, Investigation, Visualization. **Godino Leire**: Writing-Original draft preparation, Data curation, Supervision.**: Sánchez José Antonio**: Methodology, Conceptualization, Funding acquisition.

Declaration of competing interest

The authors declare the following financial interests/personal relationships which may be considered as potential competing interests: The authors gratefully acknowledge the funding support they received from the Spanish Ministry of Economy and Competitiveness for their support for the Research Project: Digital Solutions for Advanced Grinding Processes-GrinDTWin (PID2020-114686RB-I00).

Data availability

Data will be made available on request.

References

[1] F. Hashimoto, et al., Abrasive fine-finishing technology, CIRP Ann. - Manuf. Technol. 65 (2) (2016) 597–620, https://doi.org/10.1016/j.cirp.2016.06.003.
[2] Q. Miao, W. Ding, W. Kuang, J. Xu, Tool wear behavior of vitrified microcrystalline alumina wheels in creep feed profile grinding of turbine blade root of single crystal nickel-based superalloy, Tribol. Int. 145 (2020), 106144, https://doi.org/10.1016/j.triboint.2019.106144. December 2019.

[3] G. Guerrini, F. Lerra, A. Fortunato, The effect of radial infeed on surface integrity in dry generating gear grinding for industrial production of automotive transmission gears, J. Manuf. Process. 45 (2019) 234–241, https://doi.org/10.1016/j.jmapro.2019.07.006. March.
[4] W. Zhou, J. Tang, W. Shao, Study on surface generation mechanism and roughness distribution in gear profile grinding, Int. J. Mech. Sci. 187 (2020), 105921, https://doi.org/10.1016/j.ijmecsci.2020.105921. March.
[5] F. Klocke, et al., Abrasive machining of advanced aerospace alloys and composites, CIRP Ann. - Manuf. Technol. 64 (2) (2015) 581–604, https://doi.org/10.1016/j.cirp.2015.05.004.
[6] Q. Miao, W. Ding, W. Kuang, C. Yang, Grinding force and surface quality in creep feed profile grinding of turbine blade root of nickel-based superalloy with microcrystalline alumina abrasive wheels, Chin. J. Aeronaut. (2020), https://doi.org/10.1016/j.cja.2019.11.006.
[7] A. Naskar, A. Choudhary, S. Paul, Wear mechanism in high-speed superabrasive grinding of titanium alloy and its effect on surface integrity, Wear 462–463 (2020), 203475, https://doi.org/10.1016/j.wear.2020.203475. January.
[8] B. Kang, H. Ma, J. Li, B. Xu, Effect of grinding parameters on surface quality, microstructure and rolling contact fatigue behaviors of gear steel for vacuum pump, Vacuum 180 (2020), 109637, https://doi.org/10.1016/j.vacuum.2020.109637. March.
[9] K. Nadolny, State of the art in production, properties and applications of the microcrystalline sintered corundum abrasive grains, Int. J. Adv. Manuf. Technol. 74 (9–12) (2014) 1445–1457, https://doi.org/10.1007/s00170-014-6090-2.
[10] H. Deng, Z. Xu, Dressing methods of superabrasive grinding wheels: a review, J. Manuf. Process. 45 (May) (2019) 46–69, https://doi.org/10.1016/j.jmapro.2019.06.020.
[11] S. Malkin, N.H. Cook, The wear of grinding wheels: Part 2—fracture wear, Journal of Engineering for Industry 93 (4) (1971) 1129–1133, https://doi.org/10.1115/1.3428052.
[12] M.J. Jackson, B. Mills, Microscale wear of vitrified abrasive materials, J. Mater. Sci. 39 (6) (2004) 2131–2143, https://doi.org/10.1023/B:JMSC.0000017776.67999.86.
[13] D. Herman, J. Markul, Influence of microstructures of binder and abrasive grain on selected operational properties of ceramic grinding wheels made of alumina, Int. J. Mach. Tool Manufact. 44 (5) (2004) 511–522, https://doi.org/10.1016/j.ijmachtools.2003.10.026.
[14] D. Herman, J. Krzos, Influence of vitrified bond structure on radial wear of cBN grinding wheels, J. Mater. Process. Technol. 209 (14) (2009) 5377–5386, https://doi.org/10.1016/j.jmatprotec.2009.03.013.
[15] V.T. Thang, N.A. Tuan, N.V. Tiep, Evaluation of grinding wheel wear in wet profile grinding for the groove of the ball bearing's inner ring by pneumatic probes, J. Mech. Sci. Technol. 32 (3) (Mar. 2018) 1297–1305, https://doi.org/10.1007/s12206-018-0234-5.
[16] Q. Miao, W. Ding, Y. Gu, J. Xu, Comparative investigation on wear behavior of brown alumina and microcrystalline alumina abrasive wheels during creep feed grinding of different nickel-based superalloys, Wear 426–427 (2019) 1624–1634, https://doi.org/10.1016/j.wear.2019.01.080. January.
[17] H. Li, T. Yu, L. Zhu, W. Wang, Analysis of loads on grinding wheel binder in grinding process: insights from discontinuum-hypothesis-based grinding simulation, Int. J. Adv. Manuf. Technol. 78 (9–12) (2015) 1943–1960, https://doi.org/10.1007/s00170-014-6767-6.
[18] N. Macerol, L. Franca, H. Attia, P. Krajnik, A lapping-based test method to investigate wear behaviour of bonded-abrasive tools, CIRP Annals 71 (1) (Jan. 2022) 305–308, https://doi.org/10.1016/j.cirp.2022.04.049.
[19] Z. Cui, Y. Huang, H. Liu, Predicting the mechanical properties of brittle porous materials with various porosity and pore sizes, J. Mech. Behav. Biomed. Mater. 71 (2017) 10–22, https://doi.org/10.1016/j.jmbbm.2017.02.014. February.
[20] S. Zhang, X. Li, C. Tian, G. Guo, L. Wang, X. Liu, The design and fabrication of porous sintered grinding wheel based on Selective Laser Melting technology, J Phys Conf Ser 1074 (1) (2018), https://doi.org/10.1088/1742-6596/1074/1/012157.
[21] C. Zhenzhen, X. Jiuhua, D. Wenfeng, M. Changyu, Grinding performance evaluation of porous composite-bonded CBN wheels for Inconel 718, Chin. J. Aeronaut. 27 (4) (2014) 1022–1029, https://doi.org/10.1016/j.cja.2014.03.015.
[22] M. Bahaaddini, M. Serati, H. Masoumi, E. Rahimi, Numerical assessment of rupture mechanisms in Brazilian test of brittle materials, Int. J. Solid Struct. 180–181 (2019) 1–12, https://doi.org/10.1016/j.ijsolstr.2019.07.004.
[23] C. Zhang, et al., Determination of tensile strength by modified Brazilian disc method for nuclear graphite, Exp. Tech. 44 (4) (2020) 475–484, https://doi.org/10.1007/s40799-020-00363-y.
[24] M.R. Ayatollahi, A.R. Torabi, Failure assessment of notched polycrystalline graphite under tensile-shear loading, Mater. Sci. Eng. 528 (18) (2011) 5685–5695, https://doi.org/10.1016/j.msea.2011.04.066.
[25] Y. Belrhiti, et al., Combination of Brazilian test and digital image correlation for mechanical characterization of refractory materials, J. Eur. Ceram. Soc. 37 (5) (2017) 2285–2293, https://doi.org/10.1016/j.jeurceramsoc.2016.12.032.
[26] D. Li, B. Li, Z. Han, Q. Zhu, Evaluation on rock tensile failure of the Brazilian discs under different loading configurations by digital image correlation, Appl. Sci. 10 (16) (2020), https://doi.org/10.3390/app10165513.
[27] D.P. Saini, J.G. Wager, R.H. Brown, Practical significance of contact deflections in grinding, CIRP Annals 31 (1) (1982) 215–219, https://doi.org/10.1016/S0007-8506(07)63300-9.
[28] L.C. Zhang, T. Suto, H. Noguchi, T. Waida, APPLIED MECHANICS IN GRINDING PART II: MODELLING OF ELASTIC MODULUS OF WHEELS AND INTERFACE FORCES, 1993.
[29] R.L. Hecker, S.Y. Liang, X.J. Wu, P. Xia, D.G.W. Jin, Grinding force and power modeling based on chip thickness analysis, Int. J. Adv. Manuf. Technol. 33 (5–6) (Jun. 2007) 449–459, https://doi.org/10.1007/s00170-006-0473-y.
[30] U.S. Patnaik Durgumahanti, V. Singh, P. Venkateswara Rao, A new model for grinding force prediction and analysis, Int. J. Mach. Tool Manufact. 50 (3) (Mar. 2010) 231–240, https://doi.org/10.1016/j.ijmachtools.2009.12.004.
[31] D. Wang, P. Ge, W. Bi, J. Jiang, Grain trajectory and grain workpiece contact analyses for modeling of grinding force and energy partition, Int. J. Adv. Manuf. Technol. 70 (9–12) (Feb. 2014) 2111–2123, https://doi.org/10.1007/s00170-013-5428-5.
[32] E. Oñate, et al., A local constitutive model for the discrete element method. Application to geomaterials and concrete, Comput. Times Part Mech 2 (2) (Jun. 2015) 139–160, https://doi.org/10.1007/s40571-015-0044-9.
[33] H. Li, T. Yu, L. Zhu, W. Wang, Modeling and simulation of grinding wheel by discrete element method and experimental validation, Int. J. Adv. Manuf. Technol. 81 (9–12) (2015) 1921–1938, https://doi.org/10.1007/s00170-015-7205-0.
[34] J.L. Osa, J.A. Sánchez, N. Ortega, I. Iordanoff, J.L. Charles, Discrete-element modelling of the grinding contact length combining the wheel-body structure and the surface-topography models, Int. J. Mach. Tool Manufact. 110 (2016) 43–54, https://doi.org/10.1016/j.ijmachtools.2016.07.004.
[35] I. Iordanoff, A. Battentier, J. Néauport, J.L. Charles, A discrete element model to investigate sub-surface damage due to surface polishing, Tribol. Int. 41 (11) (2008) 957–964, https://doi.org/10.1016/j.triboint.2008.02.018.
[36] A. Spampinato, D.A. Axinte, On modelling the interaction between two rotating bodies with statistically distributed features: an application to dressing of grinding wheels, Proc. R. Soc. A 473 (Dec. 2017) 2208, https://doi.org/10.1098/rspa.2017.0466.
[37] D. André, J.L. Charles, I. Iordanoff, J. Néauport, The GranOO workbench, a new tool for developing discrete element simulations, and its application to tribological problems, Adv. Eng. Software 74 (2014) 40–48, https://doi.org/10.1016/j.advengsoft.2014.04.003.
[38] D. André, I. Iordanoff, J.L. Charles, J. Néauport, Discrete element method to simulate continuous material by using the cohesive beam model, Comput. Methods Appl. Mech. Eng. 213 (216) (2012) 113–125, https://doi.org/10.1016/j.cma.2011.12.002.
[39] Z.B. Hou, R. Komanduri, On the mechanics of the grinding process - Part I. Stochastic nature of the grinding process, Int. J. Mach. Tool Manufact. 43 (15) (2003) 1579–1593, https://doi.org/10.1016/S0890-6955(03)00186-X.
[40] S. Malkin, C. Guo, Grinding Technology: Theory and Application of Machining with Abrasives, Industrial Press Inc, 2008, https://doi.org/10.1115/1.2803278.
[41] W.B. Rowe, Wheel Contact and Wear Effects," *Principles of Modern Grinding Technology*, 2014, pp. 83–99, https://doi.org/10.1016/b978-0-323-24271-4.00005-1.
[42] H.S. Qi, W.B. Rowe, B. Mills, Experimental investigation of contact behaviour in grinding, Tribol. Int. 30 (4) (Apr. 1997) 283–294, https://doi.org/10.1016/S0301-679X(96)00057-6.
[43] Y. Zhou, M. Atwood, D. Golini, M. Smith, P.D. Funkenbusch, Wear and self-sharpening of vitrified bond diamond wheels during sapphire grinding, Wear 219 (1) (1998) 42–45, https://doi.org/10.1016/S0043-1648(98)00230-0.
[44] P. Olejnik, J. Awrejcewicz, M. Feckan, Friction Laws in Modeling of Dynamical Systems, 2017, pp. 1–48, https://doi.org/10.1142/9789813225299_0001.
[45] W. Konig, H. Follinger, Elasticity modulus of grinding wheels and its impact on their inprocess behavior, NDT E Int. 27 (1) (Feb. 1994) 54, https://doi.org/10.1016/0963-8695(94)90093-0.